

 Open access • Proceedings Article • DOI:10.1117/12.381686

Imaging spectroscopy using tunable filters: a review — [Source link](#)





Nahum Gat

Published on: 05 Apr 2000

Topics: [Spectral imaging](#), [Image processing](#), [Spectral signature](#), [Imaging spectroscopy](#) and [Optical filter](#)

Related papers:

- [Single disperser design for coded aperture snapshot spectral imaging](#)
- [Single-shot compressive spectral imaging with a dual-disperser architecture](#)
- [Medical hyperspectral imaging: a review](#)
- [Hyperspectral imaging – an emerging process analytical tool for food quality and safety control](#)
- [Multispectral color image capture using a liquid crystal tunable filter](#)

Share this paper:    

View more about this paper here: <https://typeset.io/papers/imaging-spectroscopy-using-tunable-filters-a-review-fclq6m14fr>

Imaging Spectroscopy Using Tunable Filters: A Review

Nahum Gat^a

Opto-Knowledge Systems, Inc. (OKSI), Torrance, CA.

ABSTRACT

Major spin-offs from NASA's multi- and hyperspectral imaging remote sensing technology developed for Earth resources monitoring, are creative techniques that combine and integrate spectral with spatial methods. Such techniques are finding use in medicine, agriculture, manufacturing, forensics, and an ever expanding list of other applications. Many such applications are easier to implement using a sensor design different from the pushbroom or whiskbroom air- or space-borne counterparts. This need is met by using a variety of electronically tunable filters that are mounted in front of a monochrome camera to produce a stack of images at a sequence of wavelengths, forming the familiar "image cube". The combined spectral/spatial analysis offered by such image cubes takes advantage of tools borrowed from spatial image processing, chemometrics and specifically spectroscopy, and new custom exploitation tools developed specifically for these applications. Imaging spectroscopy is particularly useful for non homogeneous samples or scenes. Examples include spatial classification based on spectral signatures, use of spectral libraries for material identification, mixture composition analysis, plume detection, etc. This paper reviews available tunable filters, system design considerations, general analysis techniques for retrieving the intrinsic scene properties from the measurements, and applications and examples.

Keywords: electronically tunable filter; hyperspectral; multispectral; true color vision; medical imaging; precision agriculture; archaeology; art restoration; target detection; image understanding; plume detection.

1. INTRODUCTION

Spectral image cubes are analogous to a stack of pictures of an object, a sample, or a scene, where each image is acquired at a narrow spectral band. Each pixel in the image cube, therefore, represents the spectrum of the scene at that point, Fig. 1. The nature of imagery data is typically multidimensional, spanning three spatial, one spectral, and one temporal dimensions.¹ Each point in this multidimensional space is described by the intensity of the radiance which is emitted, reflected, or a combination of both (depending on the phenomenology under investigation). Since detector arrays in image capture devices are two dimensional at most, they can only capture two dimensions of the data at one time, and another dimension displaced in time. In mobile applications (e.g., air- or space-borne, or a moving web or a conveyor belt) a sensor builds an image cube (x - y - λ dimensions) in a pushbroom fashion, by capturing typically one spatial and the spectral dimensions in each camera frame, while the second spatial dimension is captured displaced in time. In stationary applications (e.g., a sample under a microscope) it is possible to capture two spatial dimensions in each camera frame, while the spectrum axis is displaced in time². (For rapid time-varying events, other techniques allow the construction of sensors that capture the three x - y - λ dimensions in a single camera frame.) Capturing image cubes in stationary applications can be accomplished by swapping narrow band pass filters in front of the camera lens, but a more elegant, convenient, and versatile solution is afforded by the use of electronically tunable filters (ETF).



Figure 1. Image cube obtained with a liquid crystal tunable filter; providing high spatial resolution of spectral features.

a) Correspondence: E-mail: nahum@oksi.com; www.oksi.com; phone: 310/371-4445 x237; Fax 310/796-9300.

2. TUNABLE FILTERS (TF)

1.1 Tunable filter properties

A TF is a device whose spectral transmission can be electronically controlled by applying voltage, acoustic signal, etc. An ideal tunable filter would possess the attributes listed in Table 1. In practice these attributes are only met to a limited degree and each TF technology presents advantages and disadvantages. Hence, each application should carefully consider the tradeoffs. And as shown below, users must develop working solutions that capture the best attributes of a technology, and overcome other limitations.

Table 1: Ideal tunable filter attributes.

- Minimal tunability time
- Minimal out-of-band transmission
- Minimal physical thickness
- Low power consumption
- Polarization insensitive
- Selectable bandpass
- Perfect MTF
- Insensitive to environment (e.g., ambient temperature, humidity)
- Insensitive to angle of incidence of the incoming light (wide FOV)
- Infinite spectral range
- Top hat band pass curve (see Fig. 2)
- Large aperture
- Constant bandpass
- Random access to wavelengths

Spectral tunability can be achieved in a number of ways. We discuss ETFs using examples of current and upcoming devices. To fully characterize the spectral transmission of the TF, the transmission over the complete spectral range of interest needs to be characterized when the filter is tuned to a series of spectral positions. The TF performance is described by a matrix $A = (a_{ij})$ of $L \times K$ elements, where L transmission curves are measured, each at K wavelengths, where typically $K \gg L$. Further quantitative details are discussed below, after a brief review of some ETFs.

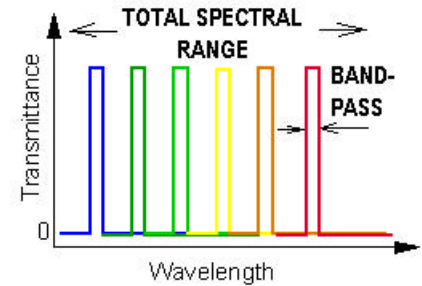


Figure 2. Ideal ETF

1.2 Electronically tunable filter examples

We discuss three classes of ETFs: liquid crystal devices based on birefringence, acousto optical devices based on diffraction, and briefly also mention the more well known interferometer type filters.

Liquid crystal tunable filter (LCTF): A Lyot-Ohman³ (or birefringent)⁴ filter, Figs. 3 and 4,⁵ is built using a stack of polarizers and tunable retardation (birefringent) liquid crystal plates. The transmission of successively thicker retardation plates is shown in Fig. 4 as curves *a, b, c*, etc. The transmission of the complete system comprising the stack is shown by the bottom curve. The LCTF is polarization sensitive. Switching speed is limited by relaxation time of the crystal and is of the order of ~50 msec. Special devices can be designed for fast switching (~5 msec) through a short sequence of wavelengths.

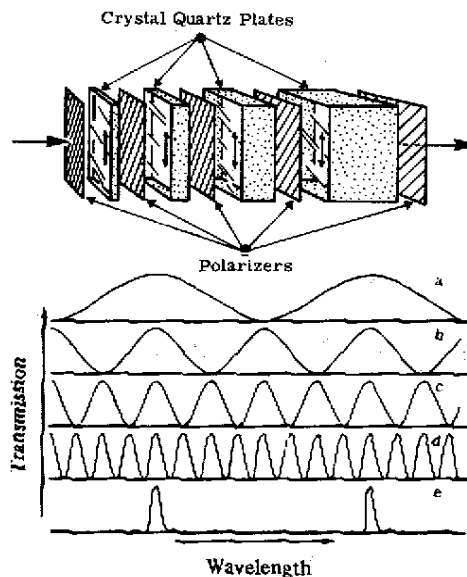


Figure 4. Operating principle of Lyot filter.

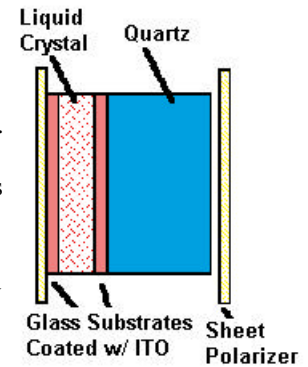


Figure 3. LCTF element.

Spectral resolution, or band pass, of the LCTF is typically of the order of several nm, although a narrower band pass can also be constructed. This is sufficient for most reflectance/transmittance analysis and even Raman measurements. Typical transmission curves are shown in Fig. 5. The band width is constant in frequency space ($\Delta\nu/\nu = \text{Const.}$) A blocking filter (e.g., a low pass with a sharp cutoff at 750 nm, in this case) is used to block the out-of-band transmission of the filter.

Holographically-formed, polymer dispersed liquid crystal (H-PDLC)⁶:

A different variation on LCTF is illustrated in Fig. 6, showing the

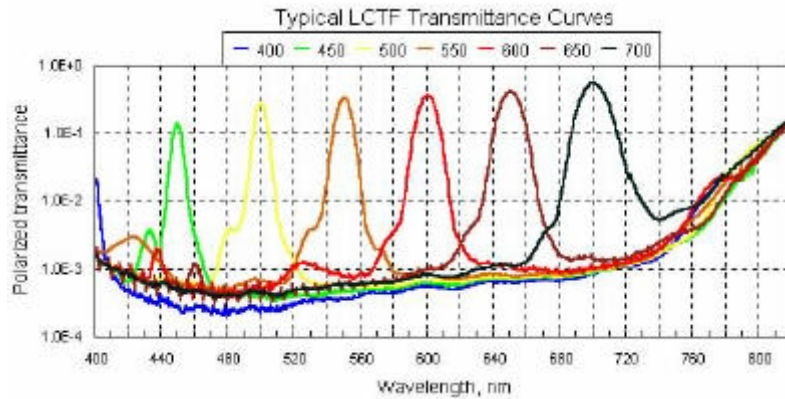


Figure 5. Transmission curves for a real LCTF.

randomly oriented and there is a mismatch in the index of refraction between the surrounding polymer and liquid crystal droplets. This condition results in a strongly scattering (opaque) appearance.⁹ By matching the ordinary refractive index of the liquid crystal with that of the surrounding polymer matrix, a transparent condition is achieved when a sufficient voltage is applied to reorient the liquid crystal droplets. Fig. 6a shows a two pixel device, where the bottom pixel is in the off-state (scattering condition) and the top pixel is in the on-state (transparent condition).

As a result of the holographic processing H-PDLCs contain a periodic array of liquid crystal droplets and solid polymer planes, Figs. 6b and c. H-PDLCs may reflect (Fig. 6b) or diffract (Fig. 6c) various wavelengths and upon application of an applied voltage the reflection or diffraction is eliminated to make the materials transparent. The reflection or diffraction wavelengths are determined by the cure conditions, and governed by electrical field controlled birefringence. Response times for H-PDLCs are of the order of $\sim 100 \mu\text{s}$.

different configurations for polymer and liquid crystal dispersions; (a) conventional PDLC; (b) reflective H-PDLC; and (c) transmissive (sometimes known as diffractive) H-PDLCs. Conventional PDLCs, Fig. 6a, are systems that capitalize on the phase separation of the liquid crystal and the evolving polymer during polymerization.^{7,8} Micron-sized liquid crystal droplets are randomly dispersed in a solid polymer binder after photopolymerization. In the zero-voltage state, the symmetry axis of the droplets is

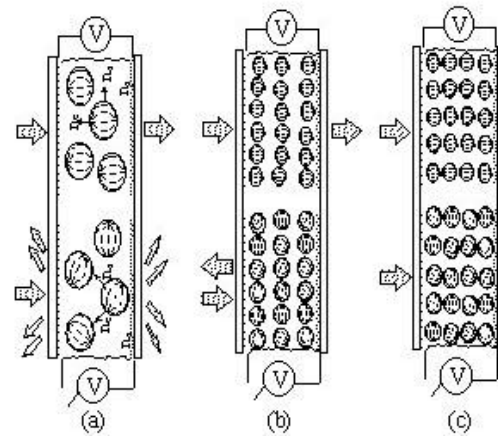


Figure 6. H-PDLC operations.

Acousto-Optic Tunable Filter (AOTF): An AOTF consists of a crystal in which radio frequencies (RF) acoustic waves are used to separate a single wavelength of light from a broadband source, Fig. 7. The wavelength of light selected is a function of the frequency of the RF applied to the crystal. Thus, by varying the frequency, the wavelength of the filtered light can be varied. The most common types of AOTFs that operate from the near UV through the short wave infrared region, use a crystal of Tellurium Dioxide (TeO_2) or Hg_2Cl_2 in a so-called non-collinear configuration — the acoustic and optical waves propagate at quite different angles through the crystal. An RF transducer, bonded to one side of the TeO_2 crystal, emits acoustic waves. As these acoustic waves pass through the TeO_2 , they cause the crystal lattice to be alternately compressed and relaxed. The resultant density changes, produce refractive index variations that act like a transmission diffraction grating or Bragg diffracter. Unlike a classical

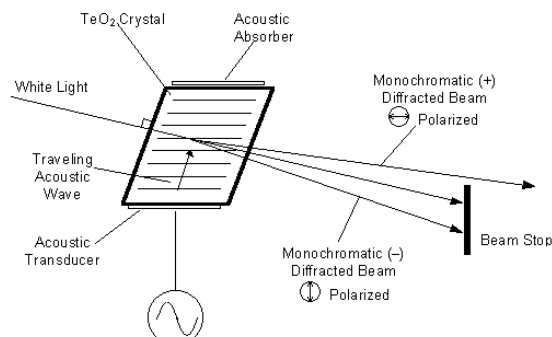


Figure 7. AOTF operations.

diffraction grating, however, the AOTF only diffracts one specific wavelength of light, so that it acts more like a filter than a diffraction grating. This is due to the fact that the diffraction takes place over an extended volume, not just at a surface or plane, and that the diffraction pattern is moving in real time. The diffracted light intensity is directed into two first order beams, termed the (+) and (-) beams, orthogonally polarized, both of which are utilized in certain applications. To use the AOTF as a tunable filter, a beam stop is used to block the undiffracted (zero order), broadband light and the (+) and/or (-) monochromatic light is directed to the camera. The angle between the beams is a function of device design, but is typically a few degrees. The bandwidth of the selected light

depends on the device and the wavelength of operation, and can be as narrow as 1 nm FWHM. Transmission efficiencies are high (up to 98%), with the intensity divided between the (+) and (-) beams. AOTFs can also be of collinear type depending on the AO crystal used to fabricate the cell (typically with crystals such as quartz, lithium niobate, etc.), where the incident and diffracted light and acoustic waves travel in the same direction. The polarization of the incident and diffracted beams are orthogonal, and the two beams are separated by using a set of polarizers.

Operations in the long wave infrared (LWIR) require special materials operating at cryogenic temperatures.^{10,11} TAS (Ti_3AsSe_3) is one material of choice, although difficult to work with due to cryo-cooling requirements.

Interferometers: A number of interferometers have been used as ETF in similar applications. These devices produce an extremely high spectral resolution and may be more appropriate for gas/plume detection tasks; a few examples follow. Fourier Transform Spectrometers (FTS) have been used in imaging modes^{12,13}, often, though, with a small number of spatial pixels. Various forms of Fabry-Perot (F-P)^{14,15,16}, etalons and liquid crystal F-P (LCFP)^{17,18}, have been used in imaging spectrometry. Micro electro manufacturing (MEM) technology promises small scale integration of F-P or FTS filters on a chip, simplifying the overall sensor design. Other application specific imaging techniques worth mentioning, include the Shearing Interferometer,¹⁹ pressure modulated gas filtering,²⁰ and gas correlation spectroscopy.²¹ The linearly variable filter (LVF), although non tunable, is also a useful spectral imaging device.

3. SYSTEM INTEGRATION CONSIDERATIONS

Successfully employing ETF for spectral imaging requires a “systems” approach in selecting optimal configuration and components. Issues to consider include camera selection, optics, data acquisition, and software integration. The intended application establishes the operating environment and parameters from which performance requirements are derived. Several typical configurations at use at OKSI are shown in Fig. 8.

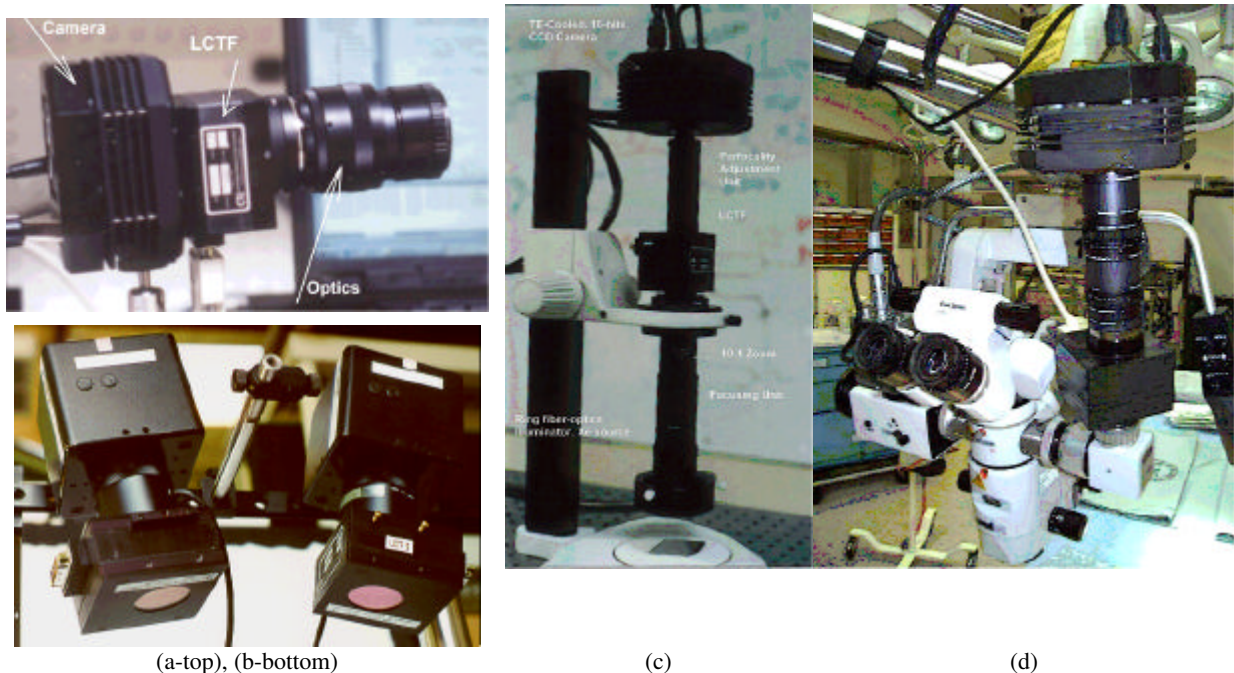


Figure 8. LCTF camera configurations: (a) LCTF mounted in front of a CCD with a long back working distance optics, (b) stereo system with apochromatic C-mounted lenses between LCTF and camera, (c) LCTF mounted within a shortened microscope tube to compensate for the optical length of the filter, and (d) a system mounted on a surgical microscope including macro reimaging optics.

The application of course determines the useful spectral range for the phenomenology under investigation. We can conveniently divide all systems into those that operate in the UV and VNIR, based on Si CCD technology, and those in the longer wavelength range. The range up to 1.7 μm may be served by InGaAs cameras. In the SWIR, HgCdTe

or InSb cameras can be used, and in the MWIR and LWIR, InSb and HgCdTe systems must be used. With the exception of the CCD and InGaAs spectral range, system cost will be significant primarily due to the required customization. In the VNIR range, CMOS cameras can be used but only for the low end applications.

Illumination is almost always a primary issue. Incandescent sources exhibit a spectral output that is low in the “blue” portion of the spectrum, and high in the near infrared (NIR). CCD’s quantum efficiency (QE) curves are typically poor in the blue and peak in the red. Throughput properties of an ETF also exhibit a certain spectral curve; for instance, low transmission in the blue and higher in the NIR, for an LCTF. Hence under such conditions we may suffer from a compound effect of overall low performance in the blue. This situation may be alleviated by selecting a CCD that has higher QE in the blue; for example, a thinned, back illuminated CCD. But there is a cost penalty associated with a high performance camera. If one can control the lighting, e.g., use a high power Xe source, a sufficient solution may be provided. Another way to improve performance in the blue, is by increasing exposure time, as $SNR \propto t^{1/2}$. This, however, requires a cooled CCD with very low dark current performance. Long exposure time may not be appropriate, though, in applications where the scene is changing on a time scale of the acquisition. One should not forget, of course, the polarization considerations when selecting light sources. Most incandescent and gas discharge sources do not emit polarized light; it is the reflection from or transmission through certain materials that may introduce polarization.

The dynamic range is another important consideration. Whereas the illumination in a laboratory environment can be well controlled, natural scenes often contain a wide range of illumination. In most cases 8 bits (256:1) is insufficient for recording the full range of natural scenes. At least 10 or 12 bits are required to cover the range, and although 16 bits would be an overkill, it may be nice to have to avoid saturation and blooming near occasional specular reflections from a scene. A clever use of exposure control, the aperture, and ADC range can overcome higher scene illumination variability.

Optics for a spectral imaging system also require special consideration. The optical thickness of many devices is greater than the back working distance of common lenses (e.g., 17.5 mm for C-mount or 46.5 mm for F-mount). Using a common lens is possible if focusing to infinity is not needed. Otherwise a special optical train is required to relay the image through the ETF. Fig. 8a shows a system with a long back working distance optics. In Fig. 8d, the system uses relay optics between the TF and the camera. In some cases the TF may be mounted in front of the optics, Fig. 8c, an arrangement that requires a large TF aperture to prevent severe vignetting. Of course the optical system should be chromatically corrected over the spectral range of interest. Finally, to reduce spectral distortion due to wide field of view, fast lenses may be preferred. In that regard, the image side of lenses may be faster than the object side, suggesting mounting the optics in front of the TF. It must be noted that due to the relatively limited selection of off-the-shelf optics for this application, one must be ready to deal with a variety of standards such as T, T2, C, F, and many more types of mechanical lens mounts, including English, and metric threads and other custom mounts.

Software is often the major effort in integrating a functional, user friendly system. The process of acquiring an image cube, should for most applications, be completely automated. This means the software application controls the camera, the TF, and data acquisition. Often there is a need to synchronize the system to an external event so that each frame is captured in sync with the object under examination.

Finally a word regarding file sizes is in order. The size of an image cube covering the spectral range from 400 nm to 1,000 nm, in 10 nm intervals, with 512×512 pixels spatial dimensions, and digitized to 12 bits (stored as 2 bytes) is



Figure 9. A portable spectral imaging system uses a laptop with a docking station to accommodate up to 3 PCI boards for frame capture, additional serial card, and an ethernet card.

32 Mbytes, excluding header information. Generous disk space must be anticipated when using such applications. These images do not compress very well using lossless techniques. The use of lossy methods must be carefully examined depending on the application.²² Data rate considerations depend on the required frame rate, but ultimately is dictated by the camera interaction with the computer bus. Low SNR often translates to a lower frame rate.

An example of LCTF system integration²³ at OKSI is shown in Figs. 9 thru. 11. For portability purposes, the system is hosted in a laptop PC attached to a docking station. The software to operate the system can be run as a stand alone application, or from within a spectral image analysis application (as a DLL). The user can select a palette, a list of colors or wavelength, for the image cube. Each palette entry can have its unique exposure time, to maximize the dynamic range of the images. An exposure time correction is then accomplished as discussed in Section 4. The user can edit the palette and preview the images at each palette entry. Once satisfied, the software loads the palette entries to the LCTF controller, and proceeds with capturing the sequence of images. If a new image cube is acquired using the same palette entries, there is no need to reload the data to the LCTF.

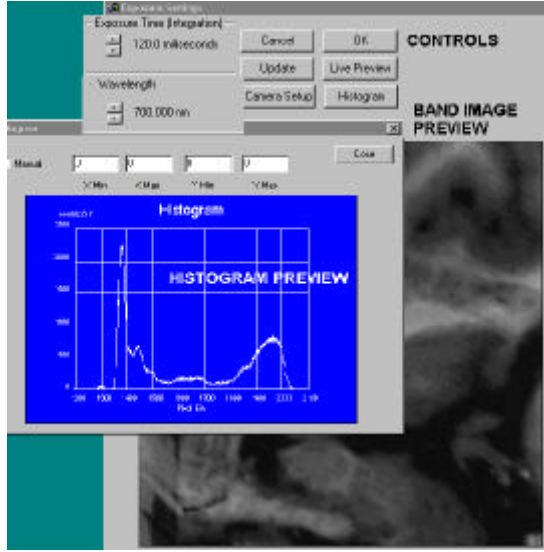


Figure 10. LCTF preview menu.

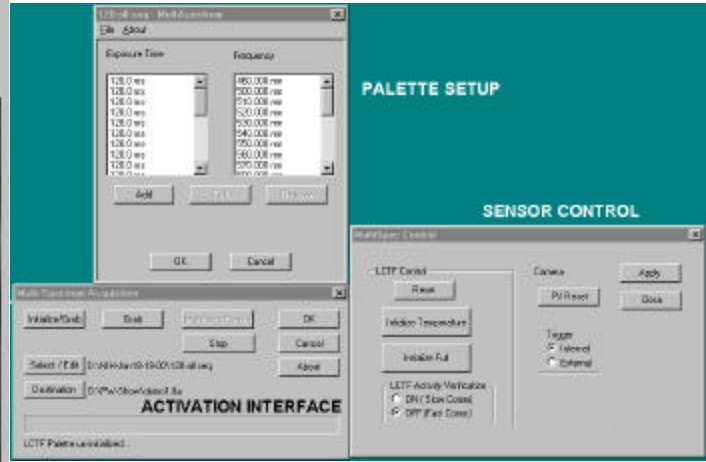


Figure 11. Software integration includes palette (band) list and corresponding exposure time, a preview widget for adjusting the wavelength and exposure time, and a "capture" button.

4. ANALYSIS

The objective of the analysis, supporting the hardware configurations shown above, is to recover the spectral reflectivity at each pixel of the scene at L spectral bands. Typical measurement geometry and sensor configuration are depicted in Fig. 12. Typically the sensor collects a sequence of images at L bands, forming an image cube with radiance or intensity value, s , associated with each x - y - λ point. Each plane in the cube may have a specific exposure time selected to optimize the dynamic range of the measurement.

Ideal TF Analysis: We conduct this analysis for an arbitrary pixel in the x - y image. The same analysis applies for each individual pixel. The unknown to be extracted from the measurements of s , is the spectral reflectivity of the scene $\rho(\lambda_j)$, $j=1, \dots, L$. Using bold face letters to designate vectors, and capital letters for matrices, the spectral signal received at a particular pixel (and each pixel has it's own set of values) can be expressed as:

$$s_{\lambda p} = t_{\text{intg}}^p(\lambda) [\mathbf{b}(\lambda) \cdot \mathbf{q}(\lambda) \cdot \tau_{TF}(\lambda) \cdot \tau_O(\lambda) \cdot \mathbf{r}_{CCD}(\lambda) \cdot \tau_{BLK}(\lambda) \cdot \Delta\lambda + \mathbf{dc}] + \mathbf{of}$$

$$= \mathbf{x}(\lambda) \cdot \mathbf{q}(\lambda) \cdot \mathbf{a}(\lambda) + \mathbf{dco}$$

Where

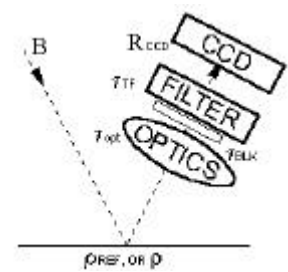


Figure 12. Measurement geometry.

(1a,b)

$$\begin{aligned}
x(\lambda) &= t_{intg}^p \cdot b(\lambda) \cdot \tau_o(\lambda) \cdot r_{CCD}(\lambda) \\
a(\lambda) &= \tau_{TF}(\lambda) \cdot \tau_{BLK}(\lambda) \cdot \Delta\lambda \\
dco &= dc \cdot t_{intg}^p + of
\end{aligned} \tag{2a,b,c}$$

In Eq. 1, from left to right, the terms include: $s = (s_1, \dots, s_L)^T$ total signal (in DN) when the TF is tuned to a sequence of wavelengths λ_p ($p=1 \dots L$); integration time ($t_{intg}=t_1, \dots, t_L$)^T; a group ($x=x_1, \dots, x_L$)^T of quantities describing the source and camera/optics properties [including source spectral radiance ($b=b_1, \dots, b_L$)^T, responsivity of each pixel in the CCD ($r_{CCD}=r_1, \dots, r_L$)^T, transmission of optics ($\tau_o=\tau_{o,1}, \dots, \tau_{o,L}$)^T that includes geometrical effects that contribute to vignetting]; reflectivity of scene pixel ($p=p_1, \dots, p_L$)^T, typically the object of the measurement; a characteristic group ($a=a_1, \dots, a_L$)^T describing the TF [including transmission of TF ($\tau_{TF}=\tau_{TF,1}, \dots, \tau_{TF,L}$)^T, the transmittance of an out-of-band blocking filter ($\tau_{BLK}=\tau_{BLK,1}, \dots, \tau_{BLK,L}$)^T, the TF bandpass ($\Delta\lambda=\Delta\lambda_1, \dots, \Delta\lambda_L$)^T at each spectral position]; the dark current (dc) flux per unit time per pixel; and an offset bias (of). Angular effects are intrinsically included via coupling to the $f/\#$ of the optics.

It is noted that in practice not all the terms in Eq. 1 are known so that additional measurements are required. The multiplicative nature of the relations allows us to lump several parameters together, as in Eq. 2, since we do not need to know the individual values but only their product.

Dropping the wavelength in the notations, yet remembering that all parameters are function of λ , we rewrite Eq. 1b:

$$s = x \cdot q \cdot a + dco \tag{3}$$

In order to retrieve the unknown of interest, p , two additional measurements are performed; “bright field cube” (s^B) and “dark field cube” (s^D). For the former we use a known reflectance reference standard (e.g., Spectralon®) p^R (≈ 1 typically for all λ 's in the VNIR), while for the latter we completely block the incoming light.

$$\begin{aligned}
s^B &= x \cdot q^R \cdot a + dco \\
s^D &= dco
\end{aligned} \tag{4a,b}$$

Using Eqs. 3, 4a and 4b we solve for the unknown spectral reflectance:

$$q = q^R \frac{s - s^D}{s^B - s^D} \tag{5}$$

This is the common two-point correction. It is noted that the TF and other sensor properties cancel out and are not required in the solution. The spectral reflectance is simply expressed in terms of the spectral measured cubes.

Real Filter Analysis: Eq. 5, derived for an ideal filter, does not account for the TF out-of-band transmission. In practice, as shown in Fig. 5, because of out-of-band transmission, the target reflectivity at **all** wavelengths contributes to the total collected signal at λ_p . For such cases, the analysis must be extended to include the contribution to the signal from all the wavelengths when the TF is set to a specific wavelength. Eq. 1 is rewritten as:

$$s = t_{intg} \left[\int_{\lambda=\lambda_1}^{\lambda=\lambda_k} b \cdot q \cdot \tau_{TF} \cdot \tau_o \cdot r_{CCD} \cdot \tau_{BLK} \cdot d\lambda + dc \right] + of, \tag{6}$$

using finite differences as:

$$\begin{aligned}
s &= t_{intg} \left[\sum_{\lambda=\lambda_1}^{\lambda=\lambda_K} \bar{b} \cdot \bar{q} \cdot \bar{\tau}_{TF} \cdot \bar{\tau}_o \cdot \bar{r}_{CCD} \cdot \bar{\tau}_{BLK} \cdot \Delta\lambda + dc \right] + of \\
s^* &= \sum_{\lambda=\lambda_1}^{\lambda=\lambda_K} \bar{x} \cdot \bar{A} \cdot \bar{q}
\end{aligned} \tag{7a,b}$$

In this case the spectral curves of the TF are divided into K intervals, and the quantities with over-bar in Eq. 7 are average quantities in the K intervals. It is important to note that the range over which the TF is characterized should cover the complete spectral sensitivity range of the camera.

The reflected (or transmitted) radiance, s , is measured at L spectral bands (positions of the TF), i.e., $s = (s_1, \dots, s_L)^T$. The source properties are described at K intervals $x = (x_1, \dots, x_K)^T$, and the TF properties are specified at K interval for each of the L wavelengths, as indicated at the top of Section 1.2.

$$\mathbf{A} = \begin{bmatrix} a_{11} & \cdots & a_{1K} \\ \vdots & \ddots & \vdots \\ a_{L1} & \cdots & a_{LK} \end{bmatrix} \quad (8)$$

It is noted that all the terms inside the brackets in Eq. 6 are vectors of K elements, whereas in Eq. 1 they were of L elements only. In Eq. 7b, $s^* = s \cdot dco$. Using the above notations we can rewrite Eq. 7 as:

$$s^* = \mathbf{A}(x \odot \varrho) \quad (9)$$

Where \odot stands for the Hadamard (term by term) product. As before, to retrieve the unknown $p = (p_1, \dots, p_K)^T$, bright field and dark field image cubes are acquired. The latter produces the dco vector as before. The former is written in terms of the reference reflectance spectrum, in a manner similar to Eq. 9.

$$s^{*B} = \mathbf{A}(x \odot \varrho^R). \quad (10)$$

Eqs. 9 and 10 can be solved to yield:

$$\varrho = [\tilde{\mathbf{A}}^{-1} s^*] \odot x^{-1} = [\tilde{\mathbf{A}}^{-1} s^*] \odot (\varrho^R) \odot [\tilde{\mathbf{A}}^{-1} s^{*B}]^{-1} \quad (11)$$

The \sim indicates an SVD inverse of \mathbf{A} as it is a non square $L \times K$ matrix where typically $K \gg L$. It is noted that L measurements were performed and the reflectance/transmittance is retrieved at K wavelengths at which the TF properties are specified.

Eq. 11 degenerates to the ideal TF solution as follows: let $a_{ij} = \begin{cases} a_{ij} \neq 0 & \text{if: } i=j \\ 0 & \text{elsewhere} \end{cases}$, and $L=K$. Hence \mathbf{A} becomes diagonal matrix, or can be represented as a simple vector \mathbf{a} containing the elements in the diagonal:

$$\mathbf{A} = \begin{bmatrix} a_{11} & 0 & 0 \\ 0 & \ddots & 0 \\ 0 & 0 & a_{LL} \end{bmatrix}, \text{ and } \mathbf{A}^{-1} = \begin{bmatrix} 1/a_{11} & 0 & 0 \\ 0 & \ddots & 0 \\ 0 & 0 & 1/a_{LL} \end{bmatrix}. \text{ Also, } [\tilde{\mathbf{A}}^{-1} s^*] = s_1^*/a_{11}, s_2^*/a_{22}, \dots, s_L^*/a_{LL}.$$

Furthermore, $[\tilde{\mathbf{A}}^{-1} s^{*R}]^{-1} = a_{11}/s_1^{*R}, a_{22}/s_2^{*R}, \dots, a_{LL}/s_L^{*R}$. Plugging all into Eq. 11, yields:

$$\begin{aligned} \varrho &= \varrho_1, \varrho_2, \dots, \varrho_L = (s_1^*/a_{11}, s_2^*/a_{22}, \dots, s_L^*/a_{LL}) \odot (\varrho_1^R, \varrho_2^R, \dots, \varrho_L^R) \odot (a_{11}/s_1^{*R}, a_{22}/s_2^{*R}, \dots, a_{LL}/s_L^{*R}) \\ &= \varrho_1^R s_1^*/s_1^{*R}, \varrho_2^R s_2^*/s_2^{*R}, \dots, \varrho_L^R s_L^*/s_L^{*R} \end{aligned} \quad (12)$$

Note: the TF properties cancel out of the equation, and the reflectivity at each band is obtained as before:

$$\varrho_j = \varrho_j^R \frac{s_j - s_j^D}{s_j^B - s_j^D} \text{ which is identical to Eq. 5.}$$

Alternate Real TF Analysis 2: The inversion of non square matrices, as in the above solution, may occasionally cause problems. The following is an alternative approach. In this approach we first use the reference reflectance cube to retrieve the illumination source properties, x , by minimizing the overall error between measurements and the model. Once known, the illumination properties are used in the model to retrieve the unknown sample reflectance p . Again, the analyses are applied to each image pixel individually.

First, we define the sum square error in all L measurements using the reference reflectance sample as in Eq. 7b:

$$\begin{aligned} \varepsilon^2 = & (\varrho_1^R \cdot a_{1,1} \cdot x_1 + \varrho_2^R \cdot a_{1,2} \cdot x_2 + \cdots + \varrho_K^R \cdot a_{1,K} \cdot x_K - s_1^{*B})^2 + \\ & (\varrho_1^R \cdot a_{2,1} \cdot x_1 + \varrho_2^R \cdot a_{2,2} \cdot x_2 + \cdots + \varrho_K^R \cdot a_{2,K} \cdot x_K - s_2^{*B})^2 + \\ & \cdots + \\ & (\varrho_1^R \cdot a_{L,1} \cdot x_1 + \varrho_2^R \cdot a_{L,2} \cdot x_2 + \cdots + \varrho_K^R \cdot a_{L,K} \cdot x_K - s_L^{*B})^2, \end{aligned} \quad (13)$$

or simply

$$\varepsilon^2 = \sum_{i=1}^L \left(\sum_{j=1}^K a_{ij} \varrho_j^R x_j - s_i^{*B} \right)^2. \quad (14)$$

Taking the derivatives of ε^2 w.r.t. each element of \mathbf{x} and equate to zero, produces K equations with the K unknowns $\mathbf{x}=(x_1, \dots, x_K)$. This system of equations has only one solution (or none).

$$\frac{\partial \varepsilon^2}{\partial x_n} = \sum_{i=1}^L \left[\left(\sum_{j=1}^K a_{ij} \varrho_j^R x_j - s_i^{*B} \right) a_{in} \varrho_n^R \right] = 0 \quad \text{for } n = 1, \dots, K. \quad (15)$$

Rewrite,

$$\sum_{j=1}^K \sum_{i=1}^L (a_{ij} \varrho_j^R) a_{in} x_j = \sum_{i=1}^L a_{in} s_i^{*B}. \quad (16)$$

Eq. 16 can be rewritten as:

$$\mathbf{G} [\mathbf{x} \odot \varrho^R] = \mathbf{A}^T \mathbf{s}^{*B}. \quad (17)$$

Here the square matrix \mathbf{G} is:

$$\mathbf{G} = \begin{bmatrix} v_{11} & v_{12} & \cdots & v_{1K} \\ v_{21} & \ddots & \ddots & v_{2K} \\ \vdots & \ddots & \ddots & \vdots \\ v_{K1} & v_{K2} & \cdots & v_{KK} \end{bmatrix}, \quad (18)$$

where

$$v_{mn} = \sum_{i=1}^L a_{in} a_{im}, \quad (19)$$

and where $m, n = 1, \dots, K$.

The \mathbf{A} matrix and vector \mathbf{s}^{*B} are defined as before:

$$\mathbf{A} = \begin{bmatrix} a_{11} & a_{12} & \cdots & a_{1K} \\ a_{21} & \ddots & \ddots & a_{2K} \\ \vdots & \ddots & \ddots & \vdots \\ a_{L1} & a_{L2} & \cdots & a_{LK} \end{bmatrix}, \quad (20)$$

$$\mathbf{s}^{*B} = \begin{bmatrix} s_1^{*B} & s_2^{*B} & \cdots & s_L^{*B} \end{bmatrix}^T, \quad (21)$$

and similarly:

$$\varrho^R = \begin{bmatrix} \varrho_1^{*R} & \varrho_2^{*R} & \cdots & \varrho_K^{*R} \end{bmatrix}^T. \quad (22)$$

The solution for the illumination source and sensor spectral properties parameter is now:

$$\mathbf{x} = (\varrho^R)^{-1} \odot [\mathbf{G}^{-1} \mathbf{A}^T \mathbf{s}^{*B}], \quad (23)$$

where $\varrho^{-1}=(1/\varrho_1, \dots, 1/\varrho_K)$. Only a square matrix hat to be inverted in this solution.

We check now for dimensional consistency. Remembering that we have L measurements that depend on reflectance and light properties in K bands: \mathbf{G}^{-1} is $(K \times K)$, \mathbf{A} is $(L \times K)$ and therefore \mathbf{A}^T is $(K \times L)$; so $\mathbf{G}^{-1} \mathbf{A}^T$ is $(K \times L)$. \mathbf{s}^{*B} is $(L \times 1)$, so that the square brackets in Eq. 23 gives a $(K \times 1)$ vector. This vector is Hadamard-multiplied by the reflectance $(K \times 1)$ vector, so that in the final answer, \mathbf{x} is a vector of $K \times 1$ elements.

Once we have the \mathbf{x} vector, we go back to the image and solve for the unknown reflectance in the K bands.

Rewriting Eq. 17 this time for the image cube (i.e., replace ϱ^R by ϱ , and \mathbf{s}^{*B} by \mathbf{s}^*),

$$\mathbf{G} [\mathbf{x} \odot \varrho] = \mathbf{A}^T \mathbf{s}^*, \quad (17a)$$

We solve as:

$$\varrho = \mathbf{x}^{-1} \odot [\mathbf{G}^{-1} \mathbf{A}^T \mathbf{s}^*], \quad (24)$$

By substituting Eq. 23 into Eq. 24 we get:

$$\varrho = \varrho^R \odot [G^{-1} A^T s^{*B}]^{-1} \odot [G^{-1} A^T s^*] \quad (25)$$

Validation: It can be shown that this solution also degenerates to the trivial one, Eq. 5, by substituting into G and A

$$a_{ij} = \begin{cases} a_{ij} \neq 0 & \text{if: } i=j \\ 0 & \text{elsewhere} \end{cases}.$$

Typical calibration results are shown in Fig. 13 where the reflectance spectra of known color standards (Labsphere) are reproduced via the analysis outline above. In order to obtain these spectra, the dark and bright (using white reference Spectralon) image cubes were collected in addition to the sample image cube.

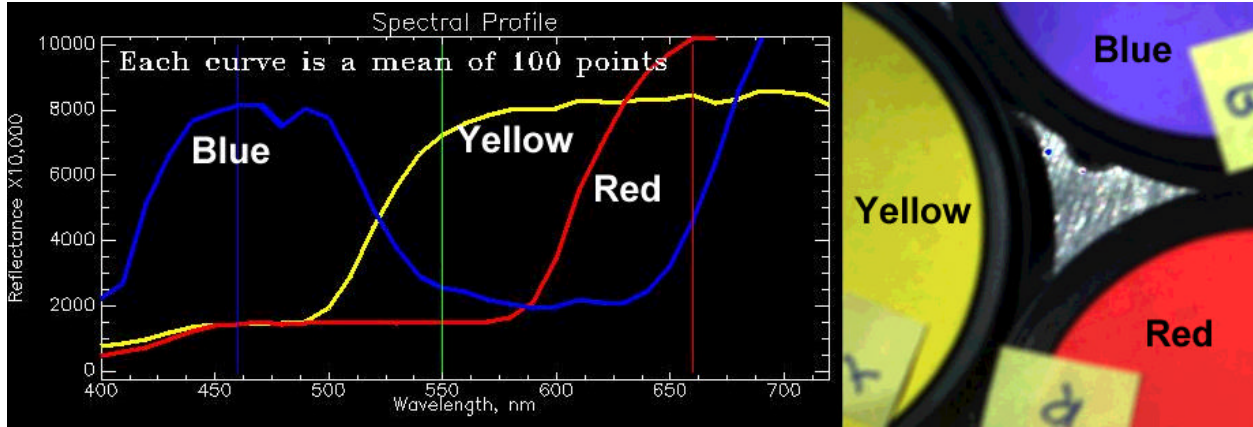


Figure 13. Color calibration samples and derived spectra using an LCTF system.

5. APPLICATIONS

In this section several applications are shown, primarily using an LCTF as an ETF. A number of references are provided for specific details of the domain in which the technology is applied. For a quantitative spectral analysis with an ETF system, one has to conduct spectral/ spatial calibration of the system. This is important since each pixel in the image will have different properties due to pixel non uniformity and, more importantly, vignetting. Thus, as indicated in Section 4, the analysis must be applied to each pixel individually. System calibration test is always a prudent step when doing quantitative analysis. In performing calibration runs, or other measurements with an LCTF, attention should be given to the polarization properties of the source and samples,²⁴ the bi-directional reflectivity distribution function (BRDF) of the sample material and its topology. The importance of these issues can not be overstated, since in most cases where results fail to meet the expectations, it is due to these factors.

Agriculture: Agriculture is moving today towards “precision farming²⁵” techniques in which crop management is performed on a local basis, rather than field wide. This requires the ability to detect and identify spatial distribution of crop stress in monoculture plots. Once identified, using multi- or hyper-spectral imaging techniques, local treatment may be applied (e.g., irrigation, fertilization, insecticide or herbicide). The approach has broad implications on production costs and the environment management. Present efforts are directed towards remote sensing applications.^{26,27,28,29} Ground truth measurements, in support of remote sensing in cotton fields, using an LCTF based camera are shown in Fig. 14a, using the configuration in Fig. 8a, and laboratory spectral analysis of cotton plants, in Fig. 15. Fig. 14b shows closed up spectral image of cotton leaves in their natural environment. In Fig. 15, the stressed leaves show reduced chlorophyll production resulting in higher reflectance in the visible than healthy leaves. Images like this allow careful study of the various spatial features of objects that can be then used to support remote sensing of similar objects. Such detailed spatial data distribution are lost when conducting field measurements with a non imaging (e.g., fiber optics) spectrometer, that integrates a significant extent of the scene.



Figure 14. (a) OKSI's LCTF system in precision agriculture ground truth validation produces images such as in (b) showing spectral details of plant canopy and soil that allow measuring spatial variability in properties in support of canopy models and remote sensing observations.

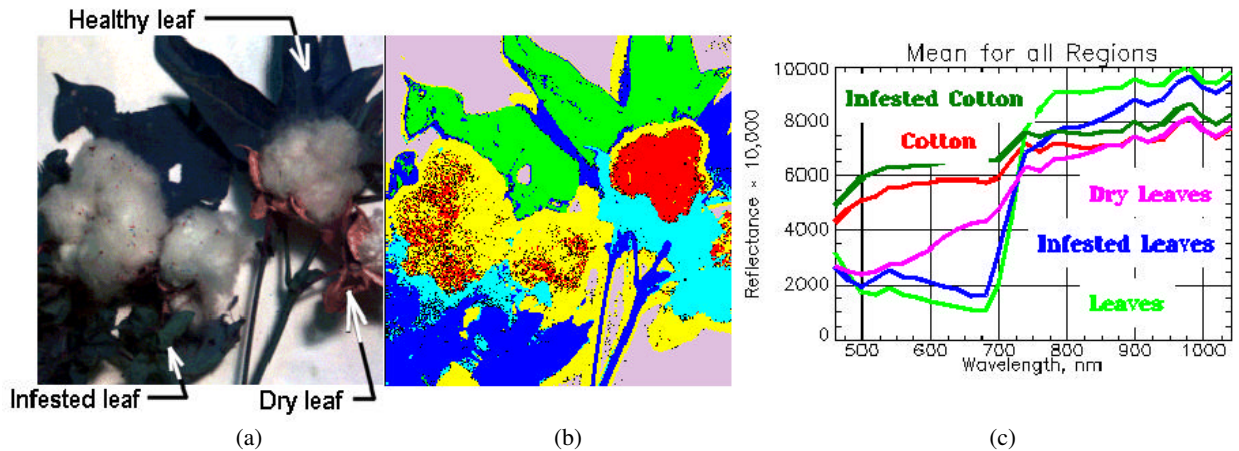


Figure 15. Laboratory hyperspectral classification of cotton leaves using a LCTF system: small samples of various components are selected (a), for a supervised classification of the remaining sample (b); the means of the classified regions corresponding to various pathologies, are plotted in (c).

Medical spectral imaging: Biological tissue exhibits unique spectra in induced³⁰ or auto fluorescence, and in transmission or reflection.³¹ Spectral differences in tissue pathology may be spatially resolved using imaging spectroscopy as shown in the following examples (the most recent conference on medical imaging includes a number of interesting papers³²). LCTF based hyperspectral imagery of dental samples (hard tissue) and of human brain during surgery are shown in Figs. 16 and 17, respectively. The latter were acquired with the system configured as in Fig. 8d where the LCTF camera is mounted onto a microscope's C-mount video camera adapter. A macro re-imaging system is attached between the LCTF and the camera. This system transfers the image formed by the microscopy inside the LCTF onto the CCD. The macro system is of a high quality to preserve the microscope performance, including chromaticity, flat field, parfocality, etc. Activity mapping of cryosectioned brain tissue was also studied with a similar system.³³

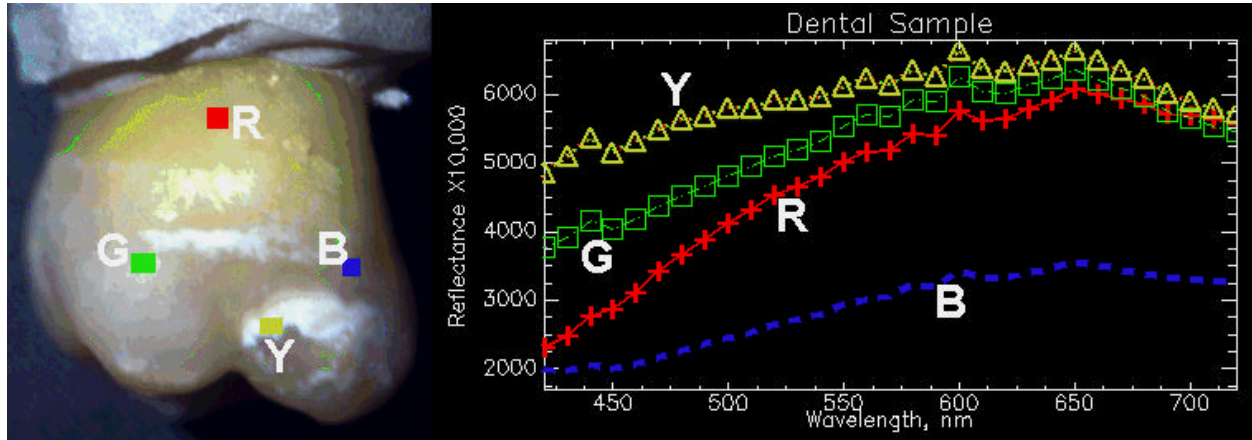


Figure 16. Dental sample in a pilot study for caries (tooth decay) diagnosis using LCTF, and the spectra of various regions on the sample that shows significant differences among the various regions on the tooth.

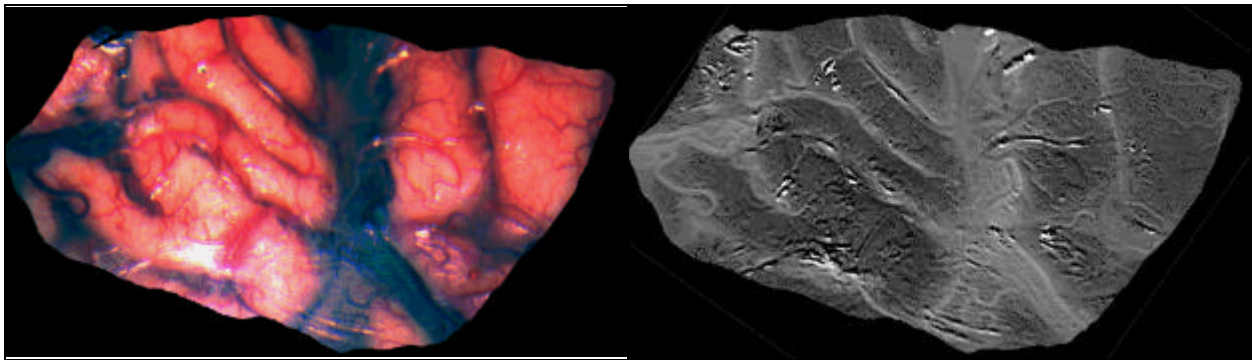


Figure 17: LCTF Brain imaging during neurosurgery (false color display R-630 nm, G-540 nm, and B-460 nm) (left), and Principal Component Transformation band that enhances the blood vessels structure (right).

Archaeology & Art: In these applications spectral analysis is used for the detection of artifacts of interest or the enhancement of faded colors or writing.^{34,35} Similarly the analysis of paintings for restoration can be aided by visible and near IR spectral imaging.

True color night vision: Another interesting application is related to generation of true color imagery under low light level (LLL) conditions. Conventional sensors for this application use image intensifiers that operate in the visible and near IR (VNIR) and produce green monochrome images. False color imagery has been generated by fusing visible light imagery from an image intensified camera with thermal infrared imagery. But such images do not help scene/image understanding since the human brain does not adapt well to false color. True color night vision is based on LLL of moonlight or starlight to generate scenes that look as they would during day time. Initial work by OKSI and Orilil produced the images shown in Fig. 18 using an LCTF in conjunction with an I2CCD camera. The true color image in the bottom right corner was generated from the individual bands using an algorithm that emulates the eye spectral sensitivity.

Other applications of imaging spectroscopy include: Human color vision, color perception³⁶ and image understanding, forensics, pharmaceutical, manufacturing, inspection, military target detection based on spectral and polarization properties^{37,38,39,40} and much more.

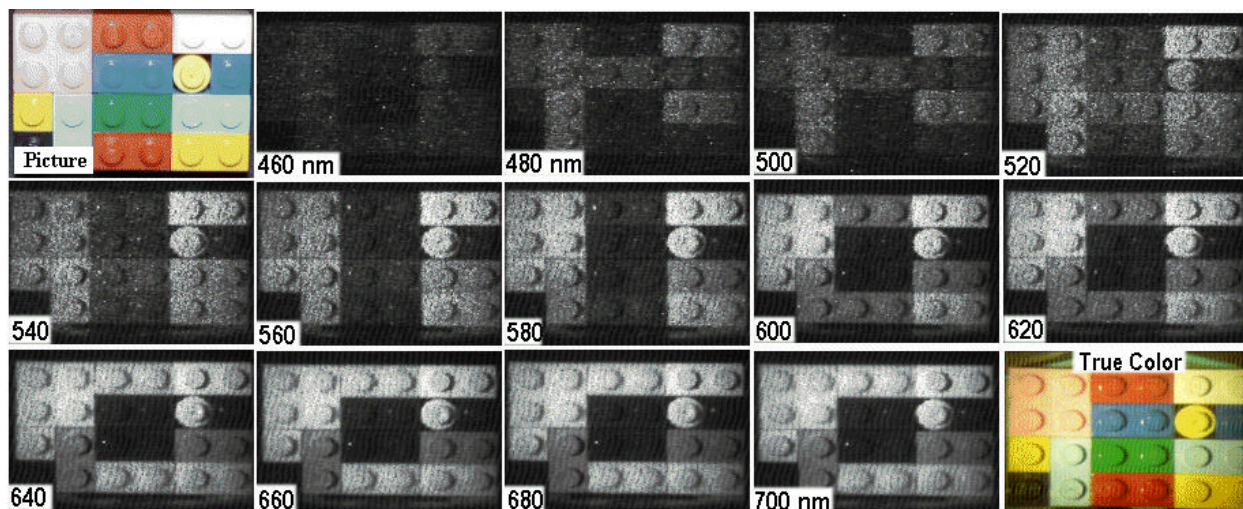


Figure 18. True color imaging under low level lighting, using an I2CCD camera: representative image cube bands, and true color reconstruction.

6. SUMMARY & CONCLUSIONS

Hyperspectral imaging technology has found many applications beyond Earth remote sensing. The combination of spatial and spectral analysis has a major advantage in applications in which, until now, few tools existed to support such work. Conventional filter wheels are slow, mechanically cumbersome, limited in color palette, and less reliable than their ETF counterparts. We have seen applications ranging from agriculture, to medicine, biology, target detection, pharmaceuticals, forensics, color vision, art restoration, archaeology, and more. ETF based systems open new opportunity for quantitative applications and research.

ACKNOWLEDGMENTS

The work described in this paper was supported in parts by NASA GSFC and NASA SSC contracts, and OKSI IR&D.

REFERENCES

1. Gat, N. "Hyperspectral Imaging," *Spectroscopy*, **14**, No.3, Pp. 28-32, March 1999 (see <http://www.oksi.com/>).
2. Gat, N. "Real-time Multi- and Hyper-spectral Imaging for Remote Sensing and Machine Vision: an Overview," paper # 983027, Presented at 1998 ASAE Annual International Mtg., Orlando, Florida, July, 1998.
3. Title, A.M., and Rosenberg, W.J. "Spectral Management," Proc. SPIE **268**, *Imaging Spectroscopy*, 1981.
4. Yeh, P., and Tracy, J. "Theory of Dispersive Birefringent Filters," Proc. SPIE **268**, *Imaging Spectroscopy* 1981.
5. Wolfe, W.L., Optical Materials, Chapter 7 in *The Infrared Handbook*, Revised Edition, 1985, Editors: Wolfe W.L., and Zissis, G.J. Published by ERIM.
6. Crawford, G.P. Private communications, 1999.
7. Crawford, G.P., Whitehead Jr. J. B., and Zumer S., *Optical Properties of Polymer Dispersed Liquid Crystals*, Taylor and Francis, London, 1997.
8. Crawford, G.P., Doane, J.W., and Zumer, S., *Polymer Dispersed Liquid Crystals and Related Systems*, Oxford University Press, Oxford, 1997.
9. Whitehead, J.B., Zumer, S., and Doane, J.W., "Light Scattering from a Dispersion of Aligned Nematic Droplets," *Journal of Applied Physics* **73**, 1057, 1993.
10. Steinbruege, K.B., Gottlieb, M., and Feichtner, J.D. "Automatic Acousto-Optical Tunable Filter (AOTF) Infrared Analyzer," Proc. SPIE **268**, *Imaging Spectroscopy*, 1981.
11. Gottlieb, M., "Ti₃AsSe₃ Noncollinear Acousto-Optical Filter Operation at 10 micrometers," *Applied Physics Letters* **34**:1, January 1979.
12. Worden, H., Beer, R., and Rinsland, C.P., "Airborne Infrared Spectroscopy of 1994 Western Wildfire," *JGR*,

102, No. D1, Pp. 1287-1299, Jan., 1997.

13. Cederquist, J.N., *et-al*, "Infrared Multispectral Sensor Program: Fourier Transform Spectrometer Sensor Characterization," Final Report # WL-TR-94-1095, May 1994 (DTIC ADA-288888).
14. Jain, A.K., *et-al*, "Dual Tunable Fabry-Perot: a New Concept for Spectrally Agile Filtering," Proc. SPIE **268**, *Imaging Spectroscopy* 1981.
15. Atherton, P.D., *et-al*, "Tunable Fabry-Perot Filters," *Optical Engineering*, **20**, No.6, Pp. 806-814, Nov/Dec. 1981.
16. Reay, N.K., and Pietraszewski, K.A.R.B., "Liquid Nitrogen-Cooled Servo-Stabilized Fabry-Perot Interferometer for Infrared," *Optical Engineering*, **31**, No.8, Pp. 1667-1670, Aug., 1992.
17. Gunning, W., Pasko, J., and Tracy, J., "A Liquid Crystal Tunable Spectral Filter: Visible and Infrared Operations," Proc. SPIE **268**, *Imaging Spectroscopy* 1981.
18. Morita, Y., and Johnson, K.M., "Polarization-insensitive tunable liquid crystal Fabry-Perot filter incorporating polymer liquid crystal waveplates," Proc. SPIE **3475**, *Liquid Crystals II*, 1998.
19. Esplin, R.W., *et-al*, "Tunable Optical Filter Using an Interferometer for Selective Modulation," Proc. SPIE **268**, *Imaging Spectroscopy* 1981.
20. McCleese, D.J., *et-al*, "Remote Sensing of the Atmosphere of Mars using Infrared Pressure Modulation and Filter Radiometry," *Applied Optics*, **25**, No.23, Pp. 4232-4245, Dec., 1986.
21. Gat, N., Realmuto, V., Unpublished work. see <http://www.oksi.com> (SO₂ camera).
22. Subramanian, S., Gat, N., Ratcliff, A., and Eismann, M. "Real-time Hyperspectral Data Compression using Principal Components Transformation," Presented at the AVIRIS Earth Science and Applications Workshop, Pasadena, CA. Feb., 2000. <http://makalu.jpl.nasa.gov/docs/workshops/toc.htm>.
23. <http://www.oksi.com>.
24. Flasse, S.P., Verstraete, M.M., Pinty, B., and Bruegge, C.J. "Modeling Spectralon's Bidirectional Reflectance for In-Flight Calibration of Earth-Orbiting Sensors," Proc. SPIE **1938**, *Recent Advances in Sensors, Radiometric Calibration, and Processing of Remotely Sensed Data*, April 1993.
25. Gat, N. *et-al*, "Application of Low Altitude AVIRIS Imagery of Agricultural Fields in the San Joaquin Valley, CA, to Precision Farming," presented at the 1999 AVIRIS workshop, http://makalu.jpl.nasa.gov/docs/workshops/99_docs/24.pdf, JPL, Pasadena, CA Feb. 1999.
26. Faust, J., Chrien, T.G., Bearman, G.H., "Multispectral imager for the agricultural user," Proc. SPIE **2345**, *Optics in Agriculture, Forestry, and Biological Processing*, pp. 412-413, Boston, MA, Nov. 1994
27. Mao, C. "Hyperspectral Imaging System with Digital CCD Cameras for both Airborne and Laboratory Application," 17th Biennial Workshop on Color Photography and Videography in Resource Assessment, ASPRS mtg., Reno, NV, May 5-7, 1999.
28. Thai, C.N., Evans, M.D., and Grant, J.C. "Herbicide Stress Detection using Liquid Crystal Tunable Filter," Paper # 973142, *ASAE Annual International Mtg.*, Minneapolis, MN, Aug. 1997.
29. Thai, C.N., Evans, M.D., and Schuerger, A.C. "Spectral Imaging of Bahia Grass Grown Under Different Zinc and Copper Treatments," Paper # 993171, presented at *ASAE Annual International Mtg.*, Toronto, Canada, July 1999.
30. Svanberg, S.M.K., and Svanberg, S. "Multicolor Imaging and Contrast Enhancement in Cancer-Tumor Localization using Laser-Induced Fluorescence in Hematoporphyrin-Derivate-Bearing Tissue," *Optics Letters*, **10**, No.2, Pp. 56-58, Feb. 1985.
31. Barlow, C.H., Burns, D.H., and Callis, J.B. "Breast Biopsy Analysis by Spectroscopic Imaging," in *Photon Migration in Tissue*, Chance, B., Ed., Pp. 111-119, Plenum Press, New York, 1990.
32. SPIE conference 3920 "Spectral Imaging: Instrumentation, Applications, and Analysis," Photonics West, San Jose, CA, January 2000.
33. Holmes, C.J., Bearman, G.H., Faust, J., Biswas, A., and Toga, A. W. "A Paler Shade of White: Multispectral Tissue Classification of Blockface Images During Human Brain Cryosectioning," *Human Brain Mapping Conference* (Copenhagen), 1997.
34. Bearman, G.H., and Spiro, S., "Archeological Applications of Advanced Imaging Techniques," *Biblical Archaeologist* 59(1):56-66, 1996.
35. Bearman, G.H., Zuckerman, B., Zuckerman, K., and Chiu, J., "Multispectral Imaging of Dead Sea Scrolls and other Ancient Documents," Society of Biblical Literature (Washington), 1993.
36. Vora, P.L., Harville, M.L., Farrell, J.E., Tietz, J.D., and Brainard, D. H. "Image capture: synthesis of sensor

- responses from multispectral images,” *Proceedings of the IS&T/SPIE Conference on Electronic Imaging*, (San Jose, CA, February 1997), **3018**, 2-11 (1997).
37. Cheng, L.-J., Mahoney, J.C., Reyes, G.F., and Suiter, H.R. “Target Detection Using an AOTF Hyperspectral Imager,” *Proc. SPIE* **2237**, Pp. 251-259, 1994.
 38. Cheng, L.-J., Mahoney, J.C., Reyes, G.F., and LaBaw, C. “Polarimetric Hyperspectral Imaging Systems and Applications,” *Proceedings of the First Army Research Laboratory Acousto-Optic Tunable Filter Workshop*, ARL-SR-54, U.S. Army Research Laboratory, Adelphi, MD, pp. 205-214, 1997.
 39. Gupta, N. “An AOTF Technology Overview,” *Proceedings of the First Army Research Laboratory Acousto-Optic Tunable Filter Workshop*, ARL-SR-54, U.S. Army Research Laboratory, Adelphi, MD, pp. 11-19, 1997.
 40. Denes, L.J., Gottlieb, M., and Kaminsky, B., “Acousto-Optic Tunable Filters in Imaging Applications,” *Opt. Eng.* **37**, pp. 1262-1267, 1998.